

7. Amin, M. S., Jalil, J. and Reaz, M. B. I., Accident detection and reporting system using GPS, GPRS and GSM technology. In International Conference on Informatics, Electronics & Vision, Dhaka, Bangladesh, 2012.
8. Sando, T., Mussa, R., Sobanjo, J. and Spainhour, L., GPS Usability in crash location. In ITE 2004 Annual Meeting and Exhibit, Lake Buena Vista, Florida, USA, 2004.
9. Sharma, S., Dashora, N., Galav, P. and Pandey, R., Cycle slip detection, correction and phase leveling of RINEX formatted GPS observables. *Curr. Sci.*, 2011, **100**(2), 205–212.
10. Song, X., Raghavan, V. and Yoshida, D., Matching of vehicle GPS traces with urban road networks. *Curr. Sci.*, 2010, **98**(12), 1592–1598.
11. Rao, G. S., Error analysis of satellite-based global navigation system over the low-latitude region. *Curr. Sci.*, 2007, **93**(7), 927–931.
12. Croyle, S. R., Spencer, L. E. and Sittaro, E. R., Vehicle navigation system and method using multiple axes accelerometer, Google Patents, 2001.
13. Goel, M., Electret sensors, filters and MEMS devices: New challenges in materials research. *Curr. Sci.*, 2003, **85**(4), 443–453.
14. Chaves, S. M., Using Kalman filtering to improve a low-cost GPS-based collision warning system for vehicle convoys, The Pennsylvania State University, USA, 2010.
15. Won, S.-h. P., Melek, W. W. and Golnaraghi, F., A Kalman/particle filter-based position and orientation estimation method using a position sensor/inertial measurement unit hybrid system. *IEEE Trans. Ind. Electron.*, 2010, **57**(5), 1787–1798.
16. Chan, C.-Y., A treatise on crash sensing for automotive air bag systems. *IEEE/ASME Transactions on Mechatronics*, 2002, **7**(2), 220–234.
17. Zaldivar, J., Calafate, C. T., Cano, J. C. and Manzoni, P., Providing accident detection in vehicular networks through OBD-II devices and Android-based smartphones. In IEEE 36th Conference on Local Computer Networks, Bonn, Germany, 2011.
18. El-Sheimy, N., Hou, H. and Niu, X., Analysis and modeling of inertial sensors using Allan variance. *IEEE Trans. Instrum. Meas.*, 2008, **57**(1), 140–149.
19. Park, S. and Tan, C.-W., GPS-aided gyroscope-free inertial navigation systems. 2002.
20. Park, S. and Tan, C.-W., GPS-aided gyroscope-free inertial navigation systems. California Path Research Report UCB-ITS-PRR-2002-22, Institute of Transportation Studies, University of California, Berkeley, 2002.

Received 17 April 2013; revised accepted 11 April 2014

Simulation study on the photoacoustics of cells with endocytosed gold nanoparticles

Ratan K. Saha*, Madhusudan Roy and Alokmay Datta

Surface Physics and Material Science Division, Saha Institute of Nuclear Physics, 1/AF Bidhannagar, Kolkata 700 064, India

The effect of endocytosis of gold nanoparticles (AuNPs) on photoacoustic (PA) signal is examined using computer simulations. It assumes that the endocytosed AuNPs significantly enhance cellular optical absorp-

tion but do not alter thermophysical parameters. The PA signals were computed employing a theoretical model at various cell and intracellular NP concentrations for 532 nm illumination. It was found that the PA amplitude increased linearly in both the cases. The simulation results, when the contributions from both coherent and incoherent components are included, demonstrate good agreement with published experimental results.

Keywords: Computer simulations, endocytosis, gold nanoparticles, photoacoustic signals.

NANOPARTICLES (NPs) are of profound interest in a variety of biological and biomedical studies. Several biomedical imaging modalities use different nanoscale structures such as gold (Au) nanospheres, Au nanorods, silver nanosystems, and carbon (C) nanotubes as contrast enhancers^{1,2}. AuNPs are found to be the most suitable for various applications because of their (i) simple and fast preparation procedure, (ii) tunable light scattering and absorption properties, (iii) ability to bind with target-specific ligands (through surface roughness manipulation) and (iv) lack of toxicity¹.

Photoacoustic (PA) imaging technique has also extensively used different metallic and non-metallic NPs as contrast agents to improve its sensitivity^{3–6}. In PA imaging, a short nanosecond pulsed laser is used to irradiate a tissue sample and this induces a pressure transient due to thermoelastic expansion^{7–9}. Such a wide band pressure transient is detected employing an ultrasonic transducer. A raster scan of a 2D region is generally performed to capture PA signals, which are then utilized to generate the corresponding grey scale image. The PA image retains optical contrast of the imaging region, and central frequency of the ultrasonic detector defines resolution of the image. This technique has been widely used to gather anatomical and functional information of various small animal organs at depths beyond optical penetration depth. The administration of NPs allows the PA technique to form images of deep tissue regions with enhanced contrast and this in turn enables it to provide *in vivo* images. Moreover, the capability of the PA technique can be extended to image specific cells or molecules by appropriate surface functionalization of NPs so that they would bind with those cells or molecules and induce PA effect. Various metallic NPs have been employed for visualizing different functional and cellular/molecular processes^{10,11}. Studies have also demonstrated that C nanotubes conjugated with cyclic Arg–Gly–Asp (RGD) peptides can serve as contrast agents for PA imaging of tumours¹².

Effort has been made to calculate theoretically the PA pressure emitted by a NP surrounded by a fluid medium¹³. Chen *et al.*¹³ computed PA pressure from bare and silica-coated NPs immersed in various solvents and by comparing calculated and measured values revealed that the surrounding medium greatly influences the

*For correspondence. (e-mail: ratank.saha@saha.ac.in)

overall strength of PA pressure amplitude. Theoretical approaches to calculate PA pressure for different biomedical systems can also be found in the literature. For example, Esenaliev *et al.*¹⁴ calculated the PA pressure from blood, assuming as a solution of haemoglobin molecules, using Green's function method and compared theoretical and experimental results examining the effect of blood oxygen saturation on PA pressure. Similarly, Guo *et al.*¹⁵ empirically modelled the PA pressure generated by a tissue medium containing a large number of randomly positioned point sources and studied why speckles are greatly suppressed in PA imaging. It may be noted that in these studies it is assumed that the PA pressure is generated in the chromophore level. Further, to the best of our knowledge, PA pressure from many cells enclosing NPs has never been evaluated employing any theoretical model.

Recently, a theoretical model has been developed to study PAs for a collection of cells approximated as fluid spheres enclosing chromophores (i.e. exploits cellular aspect of tissue)¹⁶. It assumes that the light absorption takes place in the chromophore level but acoustic emission takes place at the cellular level. The PA pressure generated by a uniformly illuminated cell suspended in a non-absorbing fluid medium has been calculated using a frequency domain approach¹⁷. The resultant PA pressure from many cells has been obtained by adding the PA wave emitted by the individual cells¹⁶. This derivation ignores multiple scattering of light and acoustic waves. The framework predicted that the strength of PA emission would increase with increasing level of aggregation of red blood cells¹⁶ and this was confirmed through *in vitro* experiments¹⁸. It was also utilized to study blood oxygenation-dependent PAs¹⁹ and to investigate PAs of malaria-infected erythrocytes²⁰.

In the present study, the validity of this theoretical model investigating PAs of a collection of cells containing AuNPs is reported. The main hypothesis is that endocytosed NPs due to their strong light absorption property alter the cellular optical absorption coefficient significantly. However, the thermophysical parameters, namely, thermal expansion coefficient, compressibility and isobaric specific heat of cells remain unchanged as the NPs occupy a negligible intracellular volume compared to the volume of a cell. The simulation results show good agreement with experimental results¹¹.

The PA pressure generated by many absorbers with radius a can be expressed as a summation of interfering waves as^{13,16,17},

$$p(\mathbf{r}, \omega) = \frac{AI_0}{r} \phi e^{ik_f r} \times \sum_{n=1}^N e^{-ik_f \cdot \mathbf{r}_n}, \quad (1)$$

where $\phi = j_1(\hat{q})e^{-ik_f a} / [(1 - \hat{\rho}) \frac{\sin(\hat{q})}{\hat{q}} - \cos(\hat{q}) + i\hat{\rho}\hat{v}\sin(\hat{q})]$ with $\hat{q} = k_s a$ and $A = i\mu\beta v_s a^2 / C_P \hat{q}$. Here, μ , β and C_P are the optical absorption coefficient, thermal expansion

coefficient and isobaric specific heat for each absorber respectively; j_1 is the spherical Bessel function of the first kind of order unity, and I_0 is the intensity of the incident beam with modulation frequency ω . The notations $\hat{\rho} = \rho_s / \rho_f$ and $\hat{v} = v_s / v_f$ denote the density and acoustic wave velocity in the absorber compared to those in the ambient medium respectively. In eq. (1), $k_s = \omega / v_s$ and $k_f = \omega / v_f$ indicate the wave numbers of the acoustic wave inside and outside the PA source respectively. Here, \mathbf{r}_n , \mathbf{k}_f and N are the position vector of the n th source, the direction of the acoustic receiver and the total number of irradiated absorbers respectively. A representative diagram is shown in Figure 1. The dashed circle indicates the irradiated region containing a collection of cells. Each small circle represents a cell packaging AuNPs (filled circles).

The time-dependent PA pressure for a delta function heating pulse can be written as^{16,19,20}

$$p_{\text{NBL}}(\mathbf{r}, t) \approx \frac{AF}{2\pi r} \int_{-\infty}^{\infty} d\omega \phi e^{i(k_f r - \omega t)} \sum_{n=1}^N e^{-ik_f \cdot \mathbf{r}_n}, \quad (2)$$

where F is the fluence of the optical beam. Equation (2) represents an analytic signal whose real part provides the PA signal and imaginary part is the Hilbert transform of the real part. The contributions from all possible frequencies are summed up in eq. (2) and therefore, it is referred to as the non-band-limited (NBL) PA signal. The band-limited (BL) signal can be obtained by convolving the NBL signal with a Gaussian function and cast as²⁰

$$p_{\text{BL}}(\mathbf{r}, t) = \text{Re}(p_{\text{NBL}}(\mathbf{r}, t)) * h(t), \quad (3)$$

where $h(t) = (\xi / \sqrt{2\pi}) \exp(-\xi^2 t^2 / 2) \cos(\omega_0 t)$ and $*$ represents the convolution operation. Here $h(t)$ is the impulse response of the receiver with ω_0 and ξ as its centre frequency and bandwidth -6 dB respectively.

Equation (2) was evaluated to obtain the NBL PA signals for two types of samples. For the first type, cell concentration was varied but μ remained constant. For the second type, cell concentration was fixed but μ was

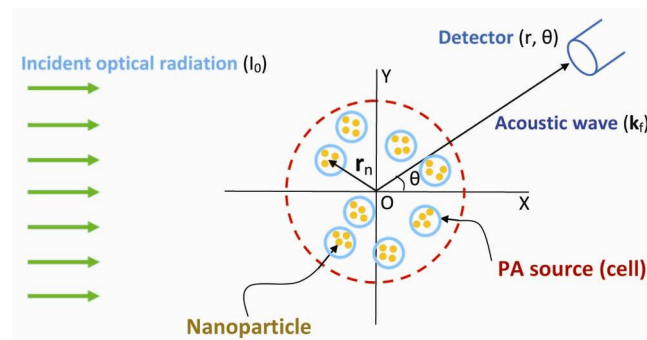
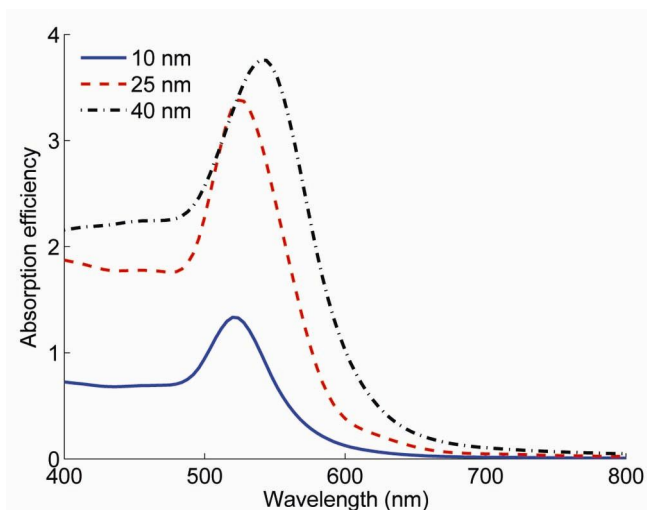
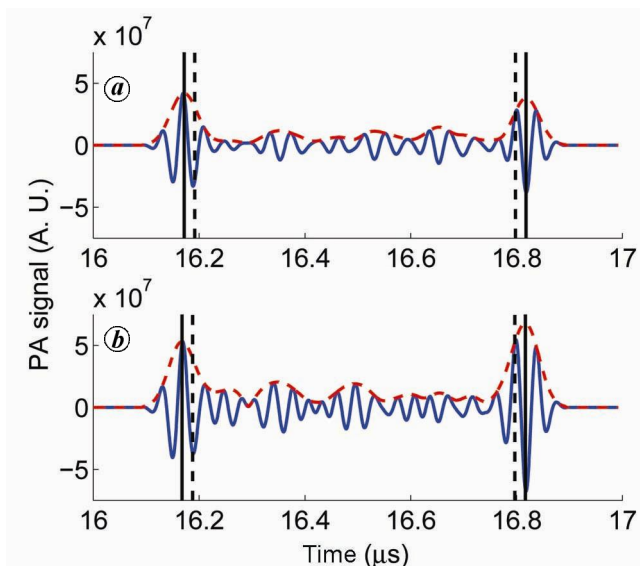


Figure 1. A schematic of the photoacoustic (PA) set-up for cells with endocytosed gold nanoparticles.

Table 1. Numerical values for cell concentration, number of nanoparticles (NPs) enclosed by a cell and estimated cellular optical absorption coefficient (μ) at 532 nm used in the simulations

Cell concentration (10^4 cells/ml)	1	5	14	20	25
NPs uptake (10^4 NPs/cell)	45.3	45.3	45.3	45.3	45.3
μ (10^2 cm $^{-1}$)	560.04	560.04	560.04	560.04	560.04
Cell concentration (10^4 cells/ml)	20	20	20	20	20
NPs uptake (10^4 NPs/cell)	1	5	10	25	45.3
μ (10^2 cm $^{-1}$)	12.36	61.81	123.63	309.07	560.04

**Figure 2.** Calculated spectra of the absorption efficiency for gold nanospheres with different radii.**Figure 3.** *a*, Computed band limited PA signal (solid line) and envelope (broken line) for 25 MHz receiver at cell concentration 14×10^4 cells/ml. Signal generated by the sample is outlined by the two outermost vertical bars (solid lines). The two innermost vertical bars (dashed lines) enclose signals from uncorrelated sources. The distance between two vertical bars (solid and dashed lines) at each boundary is about 31 μ m, which is equal to half the wavelength for the transducer centre frequency. The signals from cells situated in this region are partially correlated. *b*, Same as (*a*), but for 25×10^4 cells/ml.

altered. Cellular absorption coefficient was estimated as $\mu = c_{\text{NP}}\sigma_{\text{abs}}$, where c_{NP} is the concentration of AuNPs distributed homogeneously within the cell and σ_{abs} is the absorption cross-section for a NP. The concentration of AuNPs is given by $c_{\text{NP}} = \text{number of NPs} / \text{volume of a cell}$. The absorption cross-section is the product of absorption efficiency and geometrical cross-section of a NP. Figure 2 is a plot of the absorption efficiency curves, calculated by employing the Mie theory², for different NP sizes. The numerical values of real and imaginary parts of refractive index for Au were taken from Johnson and Christy²¹ at different optical wavelengths. Figure 2 shows that maximum for each curve reaches around 520 nm owing to surface plasmon resonance.

The size of the cell was fixed to $a = 5 \mu\text{m}$ and the cells were loaded with Au nanospheres with radius 25 nm (ref. 10). Table 1 presents various parameters considered in this study (rows 1–3 for the first type of samples and rows 4–6 for the second type). The parameter range was set based on the experiments^{10,11}.

The density and speed of sound for the extracellular matrix were taken as $\rho_f = 1005 \text{ kg/m}^3$ and $v_f = 1540 \text{ m/s}$ respectively. The same quantities for the cellular region were fixed to $\rho_s = 1090 \text{ kg/m}^3$ and $v_s = 1535 \text{ m/s}$ (ref. 22). The numerical values for β , C_p and F were considered to be unity because they determine the amplitude of a signal only. The BL signals for a transducer with 25 MHz centre frequency and 60% bandwidth (-6 dB) were simulated by computing eq. (3). Essentially it was a point detector. Experimental signals were also captured by 25 MHz focused transducer. The size of the numerical phantom was fixed to $1 \times 10 \times 10 \text{ mm}^3$. The random positions of non-overlapping cells inside the phantom were generated using a Monte Carlo technique²⁰. A laser beam (532 nm) propagated along the x -axis and signal was calculated in the backward direction. For each sample, 100 PA signals were computed from 100 independent realizations.

Figure 3*a* shows a simulated BL signal for a numerical phantom containing cells at a concentration of 14×10^4 cells/ml. The envelope of the signal is also drawn in the figure (dashed line). Two outermost vertical bars (solid lines) outline the sample region and the signal within these two bars is generated by the sample. Note that cells close to each sample surface are correlated and

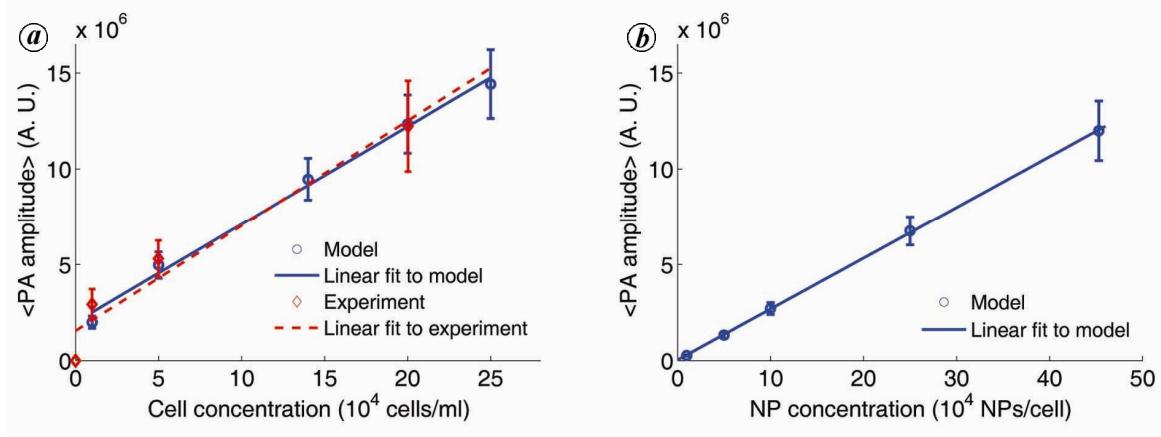


Figure 4. *a*, Variation of PA amplitude (mean \pm SD) with cell concentration at constant nanoparticle (NP) concentration (45.3×10^4 NPs/cell). Experimental data were taken from Nam *et al.*¹¹ and scaled up suitably to match the model. *b*, Plot of PA amplitude (mean \pm SD) as a function of intracellular NP concentration for fixed cell concentration at 20×10^4 cells/ml.

therefore, associated tiny signals add up coherently leading to boundary build-up. The tiny signals within the two vertical bars [solid and dashed lines, which are separated by a distance of half of the wavelength ($\sim 31 \mu\text{m}$) corresponding to the centre frequency] in each boundary have been emitted by partially correlated sources and hence their phases vary between 0 and π . However, no boundary build-up is observed in the central region due to incoherent addition of signals from uncorrelated cells located randomly in space. The origin of boundary build-up and suppression of signal amplitude in the central region have also been discussed in Guo *et al.*¹⁵. Figure 3 *b* displays a similar signal for a sample with 25×10^4 cells/ml. The PA amplitude in Figure 3 *b* is higher than that of Figure 3 *a*. It is linked to the fact that the PA amplitude increases as the concentration of the source increases.

Figure 4 *a* demonstrates the changes of the PA amplitude with concentration of cells confining AuNPs (45.3×10^4 NPs/cell). A monotonic rise of the PA amplitude can be noticed. For comparison, measured values are also plotted in the figure. Experimental data were reproduced from Nam *et al.*¹¹ (Figure 4 *a*, fluence 10.2 mJ/cm^2) and scaled up to match simulation results. Simulated trend is in excellent agreement with that of the experiment. The variation of PA amplitude with intracellular concentration of AuNPs is illustrated in Figure 4 *b*. The PA amplitude increases linearly as the NP concentration vis-à-vis μ increases. Obviously, this is because signal strength in this model is linearly proportional to μ (see eq. (1)).

In this work, the effect of bandwidth has also been investigated. A BL signal for 14×10^4 cells/ml and for a 7.5 MHz transducer with 60% as the -6 dB bandwidth is illustrated in the upper panel of Figure 5 *a*. A similar signal for 25×10^4 cells/ml and for the same transducer is shown in the lower panel of the figure. The corresponding plots for a receiver with 40 MHz as the centre fre-

quency and 60% as the -6 dB bandwidth are displayed in the upper and lower panels of Figure 5 *b* respectively. As expected, signal amplitude is greater for higher concentration of cells, and can be seen in both Figure 5 *a* and *b*. Rapid fluctuation of signal amplitude can be noticed in Figure 5 *b* due to the presence of high frequency components, whereas signal envelope looks relatively smooth in Figure 5 *a* owing to low frequency content. Additionally, signal length (within the solid and dashed bars in each boundary) corresponding to partially correlated sources is longer in Figure 5 *a* than in Figure 5 *b*. Figure 5 *c* plots variation of PA amplitude with cell concentration. The NP concentration was fixed at 45.3×10^4 NPs/cell and signals filtered with 7.5 MHz transducer were utilized in this case. A similar variation for 40 MHz transducer is shown in Figure 5 *d*. The measured values (captured by 25 MHz transducer and appropriately scaled) are also presented in the figures for comparison. Figure 5 *c* and *d* demonstrates that PA amplitude increases monotonically as the cell concentration increases as discussed earlier. It is interesting to note that the slope of the simulated trend is more than that of the experiment as shown in Figure 5 *c*, however, it is reversed in the case of Figure 5 *d*. This can be explained in the following way. For low bandwidth signals, contribution from coherent parts (enclosed by the solid and dashed lines at each boundary in Figure 5 *a*) becomes significant compared to that of incoherent part (marked by two dashed vertical bars in Figure 5 *a*). Therefore, slope of the simulated line becomes higher than that of the experiment. In the case of Figure 5 *d*, incoherent part contributes more than that of coherent part and therefore, slope of the simulated line is lower than that of the experiment.

Note that contributions from both coherent and incoherent parts were included while determining the average PA amplitude for a signal. For example, 79% of the mean amplitude is contributed by the incoherent part of the

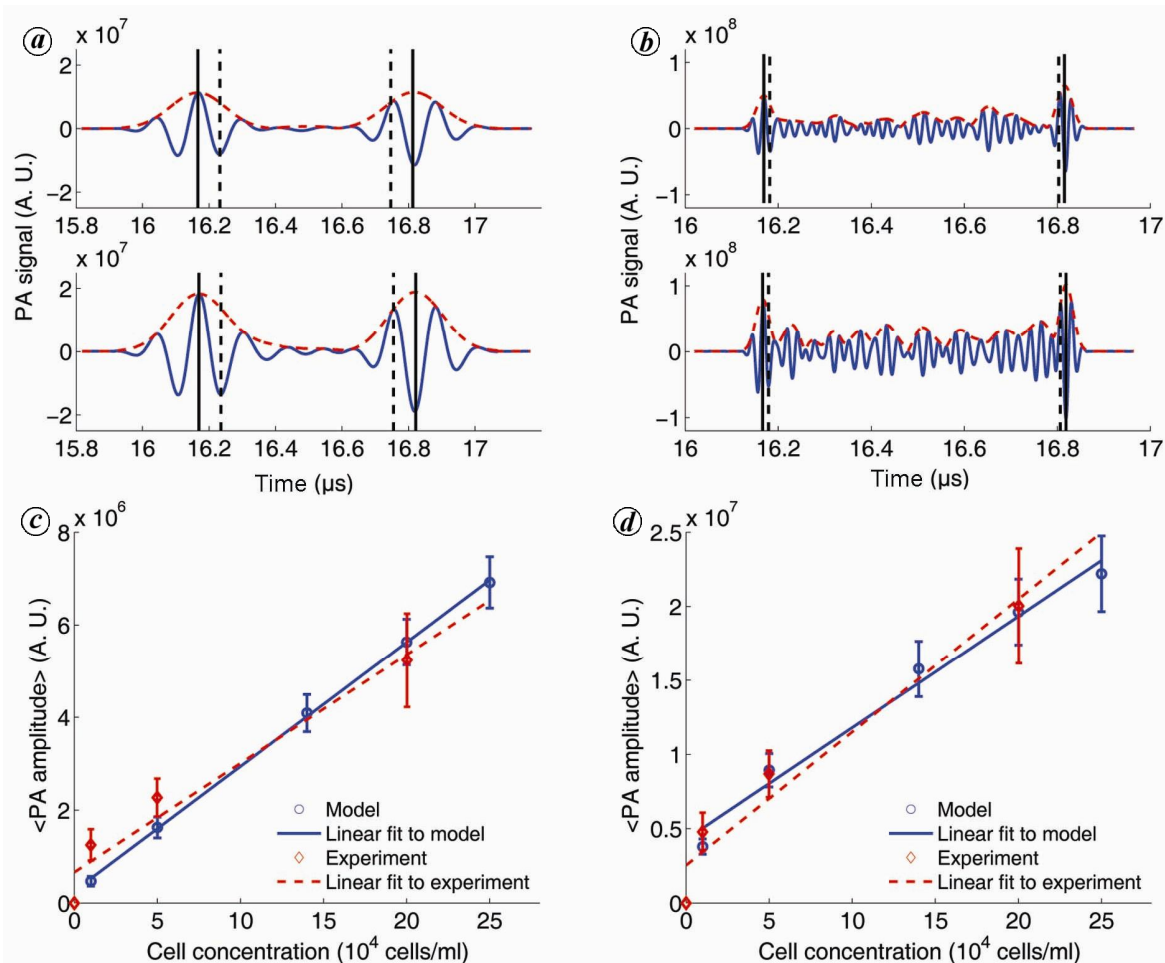


Figure 5. *a*, A simulated band limited signal generated by a sample with 14×10^4 cells/ml for a transducer with 7.5 MHz as the centre frequency and 60% as the -6 dB bandwidth (upper panel). (Lower panel) A similar signal for 25×10^4 cells/ml. *b*, Plots of the corresponding signals for a point receiver with 40 MHz centre frequency and 60% as the -6 dB bandwidth. *c*, Variation of PA amplitude (mean \pm SD) with cell concentration at a fixed NP concentration (45.3×10^4 NPs/cell) using signals filtered with 7.5 MHz detector. Appropriately scaled experimental data, detected with 25 MHz transducer, are also shown (measured values taken from Nam *et al.*¹¹). *d*, Same as (c), but using signals filtered by 40 MHz transducer.

signal enclosed by the two innermost vertical bars (dashed lines) and 21% comes from the coherent part arising from the remaining signal length (see Figure 3 *a*). Interestingly, owing to geometry of the transducer, measured signals build-up at the focal region, whereas signal strengths are minimal outside the focal region. The assumption of homogeneous distribution of AuNPs within cells is a simplification of the problem. In general, endocytosed NPs are confined in small vacuoles up to 1 μ m size, where they may have plasmonic interactions leading to considerable temperature rise due to laser irradiation altering thermophysical parameters, particularly at high laser fluence. Further investigations to include plasmonic interactions of NPs and nonlinear variation of thermal expansion coefficient into the model to address nonlinear dependence of PA signal with laser fluence are in progress. In addition, this work might be extended to develop a tool for image simulation by computing PA signals from cells

with endocytosed AuNPs for a focused transducer with finite aperture size similar to experiments^{10,11}. In conclusion, simulated trend shows excellent agreement with that of the experiment when contributions from coherent and incoherent components are taken into account and therefore, validates the suitability of this model to examine PAs of cells with endocytosed NPs.

1. Huang, X., Jain, P. K., El-Sayed, I. H. and El-Sayed, M. A., Gold nanoparticles: interesting optical properties and recent applications in cancer diagnostics and therapy. *Nanomedicine*, 2007, **2**(5), 681–693.
2. Jain, P. K., Lee, K. S., El-Sayed, I. H. and El-Sayed, M. A., Calculated absorption and scattering properties of gold nanoparticles of different size, shape and composition: applications in biological imaging and biomedicine. *J. Phys. Chem. B*, 2006, **110**(14), 7238–7248.
3. Wang, X. D., Pang, Y. J., Ku, G., Xie, X. Y., Stoica, G. and Wang, L. H. V., Non-invasive laser-induced photoacoustic

tomography for structural and functional *in vivo* imaging of the brain. *Nat. Biotechnol.*, 2003, **21**, 803.

4. Agarwal, A., Huang, S. W., O'Donnell, M., Day, K. C., Day, M., Kotov, N. and Ashkenazi, S., Targeted gold nanorod contrast agent for prostate cancer detection by photoacoustic imaging. *J. Appl. Phys.*, 2007, **102**, 064701.
5. Yang, X., Stein, E. W., Ashkenazi, S. and Wang, L. V., Nanoparticles for photoacoustic imaging. *Adv. Rev.*, 2009, **1**, 360–368.
6. Pan, D., Pramanik, M., Senpan, A., Wickline, S. A., Wang, L. V. and Lanza, G. M., A facile synthesis of novel self-assembled gold nanorods designed for near-infrared imaging. *J. Nanosci. Nanotechnol.*, 2010, **10**, 8118.
7. Beard, P., Biomedical photoacoustic imaging. *Interface Focus*, 2011, **1**, 602.
8. Zhang, H. F., Maslov, K., Stoica, G. and Wang, L. V., Functional photoacoustic microscopy for high-resolution and noninvasive *in vivo* imaging. *Nat. Biotechnol.*, 2006, **24**, 848.
9. Wang, L. V. and Hu, S., Photoacoustic tomography: *in vivo* imaging from organelles to organs. *Science*, 2012, **335**, 1458.
10. Mallidi, S., Joshi, P. P., Sokolov, K. and Emelianov, S. Y., On sensitivity of molecular specific photoacoustic imaging using plasmonic gold nanoparticles. *Proc. IEEE Eng. Med. Biol. Soc.*, 2009, 6338–6340.
11. Nam, S. Y., Ricles, L. M., Suggs, L. J. and Emelianov, S. Y., Nonlinear photoacoustic signal increase from endocytosis of gold nanoparticles. *Opt. Lett.*, 2012, **37**(22), 4708–4710.
12. Zerda, A. D. L. *et al.*, Carbon nanotubes as photoacoustic molecular imaging agents in living mice. *Nat. Nanotechnol.*, 2008, **3**, 557–562.
13. Chen, Y.-S., Frey, W., Aglyamov, S. and Emelianov, S., Environment-dependent generation of photoacoustic waves from plasmonic nanoparticles. *Small*, 2012, **8**(1), 47–52.
14. Esenaliev, R. O., Larina, I. V., Larin, K. V., Deyo, D. J., Motamedi, M. and Prough, D. S., Photoacoustic technique for noninvasive monitoring of blood oxygenation: a feasibility study. *Appl. Opt.*, 2002, **41**(22), 4722–4731.
15. Guo, Z., Li, L. and Wang, L. V., On the speckle-free nature of photoacoustic tomography. *Med. Phys.*, 2009, **36**(9), 4084–4088.
16. Saha, R. K. and Kolios, M. C., A simulation study on photoacoustic signals from red blood cells. *J. Acoust. Soc. Am.*, 2011, **129**(5), 2935–2943.
17. Diebold, G. J., Sun, T. and Khan, M. I., Photoacoustic monopole radiation in one, two and three dimensions. *Phys. Rev. Lett.*, 1991, **67**(24), 3384–3387.
18. Hysi, E., Saha, R. K. and Kolios, M. C., Photoacoustic ultrasound spectroscopy for red blood cell aggregation and oxygenation. *J. Biomed. Opt.*, 2012, **17**(12), 125006.
19. Saha, R. K. and Kolios, M. C., Effects of erythrocyte oxygenation on photoacoustic signals. *J. Biomed. Opt.*, 2011, **16**(11), 115003.
20. Saha, R. K., Karmakar, S. and Roy, M., Computational investigation on the photoacoustics of malaria infected red blood cells. *PLoS One*, 2012, **7**(12), e51774.
21. Johnson, P. B. and Christy, R. W., Optical constants of the noble metals. *Phys. Rev. B*, 1972, **6**(12), 4370–4379.
22. Falou, O., Rui, M., Kaffas, A. E., Kumaradas, J. C. and Kolios, M. C., The measurement of ultrasound scattering from individual micron-sized objects and its application in single cell scattering. *J. Acoust. Soc. Am.*, 2010, **128**(2), 894–902.

ACKNOWLEDGEMENTS. R.K.S. thanks CSIR, New Delhi for providing financial support. We thank the anonymous reviewer for suggestions that helped improve the manuscript.

Received 25 January 2014; revised accepted 2 April 2014

Monitoring of dengue and chikungunya viruses in field-caught *Aedes aegypti* (Diptera: Culicidae) in Surat city, India

Mandar S. Paingankar¹, Mangesh D. Gokhale^{1,*}, Keshav G. Vaishnav² and Paresh S. Shah³

¹Medical Entomology and Zoology Department, Microbial Containment Complex, National Institute of Virology, 130/1, Sus Road, Pashan, Pune 411 021, India

²Vector Borne Diseases Control Department, Surat Municipal Corporation, Surat 396 003, India

³Dengue Group, National Institute of Virology, 20/A, Ambedkar Road, Pune 411 001, India

A virological surveillance was carried out in various places of Surat Metropolitan Region (SMR) to monitor the chikungunya and dengue activity in *Aedes aegypti* populations. A total of 556 pools constituting 4918 *Ae. aegypti* mosquitoes were collected and processed in the laboratory for the detection of chikungunya virus (CHIKV) and dengue virus (DENV) using Immuno Fluorescence Assay (IFA) and reverse transcription polymerase chain reaction (RT-PCR). Thirteen pools were found positive for DENV and one pool was found positive for CHIKV. Molecular phylogeny results revealed that DENV-3 GIII, DENV-4 GI and CHIKV ECSA are circulating in Surat. Based on GIS information and climate conditions, the risk map for *Ae. aegypti* and DENV infections was predicted. Risk maps suggest that the central and western parts of Surat are at high risk of *Ae. aegypti* spread and associated DENV infection.

Keywords: Arboviruses, GIS mapping, phylogenetic analysis, risk map, surveillance.

DENGUE virus (DENV) and chikungunya virus (CHIKV) cause a major public health challenge in the tropical and subtropical areas of the world. The four antigenically related dengue serotypes (1–4) are responsible for dengue fever (DF) and dengue haemorrhagic fever (DHF)¹. Recently, DENV-5, phylogenetically distinct from the other four types, was detected in human patient samples from Sarawak state of Malaysia (presence of DENV-5 was announced in the Third International Conference on Dengue and Dengue Haemorrhagic Fever, Bangkok). Yearly, over 100 million cases of dengue infections worldwide are estimated to occur and have become not only a huge health problem, but also a serious economical burden in those areas which are now endemic for dengue infections. CHIKV is endemic in Africa and Southeast Asia², and millions of cases have been reported from these areas since 2005. DENV and CHIKV are transmitted by the

*For correspondence. (e-mail: gokhale40@gmail.com)